The Goldstone Real-Time Connected Element Interferometer

C. Edwards, Jr., D. Rogstad, D. Fort, L. White, and B. Iijima
Tracking Systems and Applications Section

Connected element interferometry (CEI) is a technique of observing a celestial radio source at two spatially separated antennas and then interfering the received signals to extract the relative phase of the signal at the two antennas. The high precision of the resulting phase delay data type can provide an accurate determination of the angular position of the radio source relative to the baseline vector between the two stations. This article describes a recently developed connected element interferometer on a 21-km baseline between two antennas at the Deep Space Network's Goldstone, California, tracking complex. Fiber-optic links are used to transmit the data to a common site for processing. The system incorporates a real-time correlator to process these data in real time. The architecture of the system is described, and observational data are presented to characterize the potential performance of such a system. The real-time processing capability offers potential advantages in terms of increased reliability and improved delivery of navigational data for time-critical operations. Angular accuracies of 50–100 nrad are achievable on this baseline.

I. Introduction

Interferometric techniques have been used for several decades in the astronomy community to obtain very high angular resolution images or to determine astrometric positions of celestial radio sources [1–4]. By cross-correlating signals received at two spatially separated sites, one synthesizes an effective aperture corresponding to the spatial separation of the two antennas, with a resulting improvement in angular resolution. Just as the beamwidth of a single-aperture antenna scales as λ/D, where λ is the observing wavelength and D is the antenna diameter, the resolution of an interferometer scales as λ/L, where L is the distance between the interferometer antenna pair. As will be demonstrated, this same high resolution can be used to help track and navigate interplanetary spacecraft.

Two-way tracking of the round-trip delay and Doppler shift of radio signals between Earth and a spacecraft pro-

vides a direct measurement of the geocentric range and radial velocity of the spacecraft. For current-generation spacecraft incorporating X-band (8.4-GHz) radio links, spacecraft range can be determined to 10 m, and spacecraft radial velocity to 0.1 mm/sec.

The plane-of-sky angular coordinates of the state vector, however, are more difficult to determine. Some angular information can be deduced from the signature of the Earth's rotation on the Doppler observable. Accuracies of about 150 nrad can be obtained from an 8- to 12-hr arc of Doppler data. Near the celestial equator, the accuracy of the declination component of angular position degrades as $1/\sin(\delta)$, where δ is the spacecraft declination, due to a singularity in the Doppler partial derivative.

Interferometric techniques have been developed and are used in the Deep Space Network to improve the ability to track angular spacecraft position. Currently, the technique of very long baseline interferometry (VLBI) is used in the DSN for spacecraft tracking. As shown in Fig. 1, VLBI measures angular position by determining the delay, τ, between arrival of the signal wavefront from a radio source at the two antennas. This delay is related to the angle, θ, between the baseline and the direction to the radio source:

$$\tau = \frac{1}{c} B \cos\theta \tag{1}$$

where c is the speed of light. Because of the large spatial separation between VLBI antennas, data are recorded at each antenna along with timing references from extremely stable clocks at each site. The recorded data are then transmitted to a common site for subsequent correlation processing, in which the delay is extracted. Final observables are typically unavailable until hours or days after the observation is complete.

The current DSN VLBI system can provide angular accuracies of about 30 nrad for spacecraft tracking, based on a short, 30-min observation, which represents a significant improvement over Doppler tracking alone. The VLBI observation provides a direct, geometric determination of the spacecraft angular position, in contrast to the Doppler case in which the angular position is extracted from the signature of Earth's rotation on the Doppler observable over a long data arc. In addition, VLBI suffers no degradation in accuracy at declinations near 0 deg. Combining information from the California–Spain and California–Australia DSN baselines allows good determination of both the right ascension and declination of the spacecraft throughout the ecliptic plane.

By rearranging Eq. (1), one finds that the angular accuracy $\delta\theta$ is related to the accuracy $\delta\tau$ with which the delay is determined and the length of the baseline projected onto the plane of the sky:

$$\delta\theta = \frac{c\delta\tau}{B\sin\theta} \tag{2}$$

From this, it is seen that angular accuracy is improved by improving the delay measurement or by increasing the baseline length. This latter point has driven the development of VLBI on intercontinental baselines; the DSN baselines from California to Spain and California to Australia are roughly 8000 and 10,000 km in length, a sizable fraction of the Earth's total diameter.

For several years, the authors have been investigating the extent to which interferometry on relatively short baselines of under 100 km in length can provide medium accuracy, 50- to 100-nrad angular tracking. To achieve this degree of accuracy on such a short baseline requires improving the precision of the interferometer delay measurement. As will be shown in the next section, on these shorter baselines one can make full use of the interferometer phase observable to achieve this gain in precision. In addition, there are a number of operational benefits to performing interferometry on a short baseline that have motivated interest in investigating connected element interferometry (CEI) [5]:

(1) By using fiber-optic links, the data from the various antennas can be brought together to a common site for real-time correlation processing, reducing the turnaround time for delivering tracking observables to a navigation filter.

(2) Real-time processing provides a real-time monitor of the complete interferometry system. Many problems affecting VLBI observations are not detected until correlation processing; real-time correlation would help to uncover such problems during the observation in time to correct them.

(3) A common clock can be distributed to both antennas, allowing them to be operated coherently and eliminating the need to solve for a clock rate offset between stations.

(4) Propagation media errors are significantly reduced due to common-mode cancellation on the short baseline.

(5) The short baseline results in longer mutual visibility periods and higher elevation angles. This eases observation scheduling and reduces the effect of propagation media errors.

II. The CEI Phase Observable

The basic observable of any interferometer is the relative phase of a received signal at two spatially separated antennas. This phase can be thought of as a measure of the interferometer delay τ in units of the observing wavelength. One can write the interferometer phase as

$$\phi + 2\pi N = \omega_{RF}\left(\frac{1}{c}B\cos\theta + \tau_{clock} + \tau_{trop} + \tau_{ion} + \tau_{inst}\right) + \phi_{LO} \quad (3)$$

where ω_{RF} is the RF observation frequency, and where the total delay τ is composed of the geometric delay given in Eq. (1), the clock offset between stations τ_{clock}, the tropospheric and ionospheric propagation media delays τ_{trop} and τ_{ion}, and any uncalibrated instrumental delay τ_{inst}. (Each of these delay terms represents the differential effect between stations.) In addition, there is an overall unknown phase offset ϕ_{LO} between the aggregate local oscillators at each station. The term $2\pi N$ represents the cycle ambiguity associated with the phase data type. The high precision of the phase data type is not usable until this cycle ambiguity has been properly resolved.

For VLBI, uncertainties in the delay model typically prevent resolving the phase ambiguity. Instead, the delay is measured directly by determining the group delay $\partial\phi/\partial\omega$. In practice, what is actually measured is the quantity $(\phi_1 - \phi_2)/(\omega_1 - \omega_2)$ for two or more nearby frequencies. This group delay observable provides an unambiguous, but much less precise, measure of the interferometer delay. The group delay is less precise by the ratio of $\omega/\Delta\omega$, where ω is the RF observing frequency, and $\Delta\omega$ is the spanned bandwidth over which the group delay is calculated. For an X-band (8.4-GHz) spacecraft downlink with VLBI tones spanning a 40-MHz bandwidth, the phase observable is thus more than two orders of magnitude more precise than the group delay. The inability to resolve the integer cycle ambiguity prevents the use of this precise phase observable on intercontinental baselines.

On short baselines, however, the a priori delay model is sufficiently accurate to allow phase ambiguity resolution. Biases associated with the clock, instrumental, and LO terms in Eq. (3) are handled by differencing the phase observable for two sequential radio source observations. This differencing also greatly attenuates the effects of the propagation media errors if the sources are angularly close. The differential phase observable for two sources, A and B, can then be written

$$\Delta\phi + 2\pi\Delta N = \omega_{RF}\left(\frac{1}{c}B\left[\cos\theta_A - \cos\theta_B\right] + \Delta\tau_{trop} + \Delta\tau_{ion} + \Delta\tau_{inst}\right) \quad (4)$$

where ΔN now represents the differential phase ambiguity. The term $\Delta\tau_{inst}$ is retained to represent any stochastic temporal instability in the CEI signal path over the time between the two observations.

III. CEI Error Sources

CEI error analysis focuses on two distinct issues: the a priori model delay accuracy required to achieve ambiguity resolution and the final a posteriori accuracy obtained from the resolved phase observable. The ability to determine the differential phase ambiguity ΔN is dependent on the a priori model uncertainties associated with the terms on the right-hand side of Eq. (4). Basically, the overall delay model must be known to much better than a wavelength of the RF observing frequency. The DSN downlink spacecraft frequencies of 2.3 GHz (S-band) and 8.4 GHz (X-band) correspond to wavelengths of 13 and 3.6 cm, respectively. Once the ambiguity is resolved, many of these same errors will limit the final astrometric accuracy of the observation. In the following sections, each of these error sources is briefly examined.

A. Baseline

For short intracomplex DSN baselines, the vector between stations is typically known to 3–5 mm or less, based on geodetic interferometry experiments. For small angular separations between the radio sources, the impact of this uncertainty on the differential phase delay is further reduced, roughly by the angular source separation in radians. Thus, for a 10-deg separation, this error is below 1 mm.

Gravity deformation, wind loading, and thermal expansion could also potentially introduce antenna distortions at the millimeter level. Here again, the differential nature of the CEI observations is key to reducing this error source. Angularly close sources will have similar gravity deformation; similarly, differencing observations over a short time scale will help to reduce the effects of wind and thermal distortions. Further error cancellation will occur if the two antennas used in the observation are of identical size and design.

B. Source Position

Here it is assumed that one of the sources is a well-known reference quasar with an a priori position uncer-

tainty of 10 nrad and that the other source, the target source whose position is to be determined (e.g., a spacecraft), has a much larger source position uncertainty $\delta\theta$. On a 21-km baseline (corresponding to the longest available DSN intracomplex baseline), the 10-nrad error of the reference source corresponds to a 0.2-mm error. To unambiguously determine the phase ambiguity, a priori knowledge of the target source position must satisfy

$$\delta\theta < \frac{1}{6}\frac{\lambda}{B\sin\theta}$$

where λ is the observing wavelength. The factor of 1/6 ensures that anything less than a 3-sigma position error will cause less than a 1/2-wavelength error, and thus not cause a cycle ambiguity error. For S-band observations, and a projected baseline length of 21 km, this corresponds to a required a priori position knowledge of about 1 μrad for the target source.

C. Troposphere

The troposphere error corresponds to the double difference of the tropospheric path delay along the four lines of sight from the two ground stations to the two radio sources. Most of the overall tropospheric effect cancels in this double differencing; the remainder represents the spatial and temporal fluctuations in the troposphere on a scale determined by the spatial separation of the antennas, the angular separation of the sources, the scale height of the troposphere, and the time separation of the two scans. These effects have been studied thoroughly elsewhere [6,7]; here the authors will just characterize the expected magnitude of this error source: For an angular source separation of 10 deg, a 21-km baseline, an average elevation angle of 45 deg, and a time separation of 200 sec between scans, the differential troposphere error is expected to be about 5 mm. This error grows to 10 mm when the mean elevation drops to 20 deg. Because this error is due primarily to small-scale fluctuations in the troposphere, the error is largely uncorrelated from one differential observation to the next and thus can be reduced by repeated observations.

D. Ionosphere

The ionosphere causes a dispersive phase error for each ray path of the form

$$\delta\phi_{[cyc]} = -1.34\frac{TEC_{[10^{16}\text{el/m}^2]}}{\nu_{[\text{GHz}]}}$$

where $\delta\phi_{[cyc]}$ is the phase in cycles, $TEC_{[10^{16}\text{el/m}^2]}$ is the integrated line-of-sight total electron content, and $\nu_{[\text{GHz}]}$ is the observing frequency in gigahertz. Note the minus sign: The ionosphere actually causes the phase of the wavefront to advance. Taking the derivative with respect to frequency yields a positive group delay, as required by causality. Typical daytime values of TEC can range up to $100 \times 10^{16}\text{el/m}^2$ or more at zenith and three times higher at low elevations, which corresponds to tens of cycles at X-band and 100 cycles or more at S-band. As in the case of the troposphere, however, most of this error cancels in the double-differenced CEI observable, with the residual error being due to small-scale ionospheric inhomogeneities. While theoretical understanding of these fluctuations is limited, empirical data suggest that the ionosphere error for differential CEI observations on a 21-km baseline should be at or below the millimeter level at X-band,[1] representing just a few percent of a cycle of X-band phase. At S-band, this error grows to roughly one-tenth of a cycle. This is large enough to be of concern, but should not prevent accurate phase ambiguity resolution. Given the size of this error source and the variable nature of the ionosphere, more data on ionosphere fluctuations would be welcome. Experience gained in operating the Goldstone CEI will help to evaluate the magnitude of this error. If dual-frequency S- and X-band data are available, and no cycle errors are made at either band, this dispersive error source is eliminated by forming the appropriate linear combination of S- and X-band phase delay observables, which eliminates the charged particle error:

$$\Delta\tau_{S/X} = \left(\frac{\omega_X^2}{\omega_X^2 - \omega_S^2}\right)\frac{\Delta\phi_X}{\omega_X} - \left(\frac{\omega_S^2}{\omega_X^2 - \omega_S^2}\right)\frac{\Delta\phi_S}{\omega_S}$$

E. Clocks and Instrumentation

Because a single clock is used for both stations in CEI, there is no clock rate error as in VLBI. However, there is still a clock epoch uncertainty, since the propagation delays through the frequency distribution system and through the CEI signal path itself are not calibrated at the level of an RF wavelength. Thus, the CEI phase observable contains a phase bias, which corresponds to the unknown relative phase of the local oscillators at the two stations. This bias is removed by forming differencing phase observables for two radio sources. This differencing also serves to eliminate or reduce any other biaslike errors.

[1] A. J. Mannucci, "Temporal Statistics of the Ionosphere," JPL Interoffice Memorandum 335.1-90-056 (internal document), Jet Propulsion Laboratory, Pasadena, California, October 25, 1990.

While there is no explicit clock rate term, there are instabilities in the frequency distribution system, which can lead to an apparent difference in the instantaneous reference frequency at the two stations. The delay error induced by such an instability is $T\sigma_y(T)$ where T is the time between two scans used to form a differential observable and $\sigma_y(T)$ is the Allan standard deviation on that time scale. For $T = 300$ sec and $\sigma_y(T) = 10^{-14}$, this leads to a 3-psec error; the fiber-optic clock transfer between stations is thought to be even better than this [8].

IV. Non-Real-Time Phase Delay Observations

A number of experiments have been performed on baselines within the Goldstone complex in a non-real-time mode, with data recorded separately at each station [5,9]. The goals of these experiments were to demonstrate reliable phase ambiguity resolution and evaluate the potential angular accuracy of CEI observations. The results are briefly reviewed here.

Figure 2 shows the location of existing antennas within the Goldstone, California, Deep Space Communications Complex (DSCC). Baselines of up to 21 km are available. Fiber-optic cables have been installed linking the various antenna pairs [8]. For these non-real-time experiments, such fibers were used to distribute a common frequency reference to each antenna, which allowed the separate stations to be operated coherently.

Data have been collected on the 6-km DSS-12–DSS-13 baseline and on the 21-km DSS-13–DSS-15 baseline; only the latter results are discussed here. Data were recorded at each antenna for these non-real-time experiments; correlation processing and postprocessing were performed subsequently at JPL. To simulate differential quasar–spacecraft observations, pairs of quasars were observed with angular separations of up to 20 deg. The dual frequency S-/X-calibrated observations were then used to determine the relative angular position of each quasar pair.

Ambiguity resolution was carried out as follows:

(1) An a priori delay model was calculated for each quasar observation; an ambiguous residual phase was then calculated for the S- and X-band observation relative to this model.

(2) The residual phases were differenced between adjacent scans for a given quasar pair. This serves to eliminate the unknown phase bias between stations and reduce many other errors through common-mode cancellation.

(3) The a priori delay model was used to resolve the S-band phase ambiguity for the differential phase observable. In effect, this required the a priori model for the differential quasar delay to be good to about 6.5 cm or better (1/2 the S-band wavelength).

(4) The S-band residual was then used to resolve the X-band cycle ambiguity. (The X-band ambiguity was chosen so that the S- and X-band phase delay residuals agreed to within half an X-band cycle.) This approach assumes that the dominant errors are nondispersive, which implies that the S- and X-band phase delay residuals should be the same. This permits successful X-band ambiguity resolution even when nondispersive errors are more than half an X-band cycle.

Statistical analysis of the resulting phase residuals supports the reliability of the S- and X-band phase ambiguity resolution: The raw phases cluster about integer values of the cycle ambiguity, and the width of the distribution is much less than half a cycle.

After ambiguity resolution, the S-/X-calibrated phase delay observable is formed to remove the effects of charged particles. To assess the accuracy of these phase delay observations, the data were fit to estimate the angular position of one of the quasars relative to the other. Figure 3 shows the resulting adjustment in right ascension and declination for the radio source CTA 102 for roughly 3 hours of data. The data were weighted based on a model of tropospheric fluctuations above a 21-km baseline; the observed phase delay residuals were consistent with these data weights. The semi-minor axis of the source position error ellipse is 73 nrad. While each individual measurement only provides information for one component of the plane-of-the-sky position, the baseline rotation over the full observation period allowed some determination of the orthogonal component. A second orthogonal baseline would allow better determination of both components of sky position in a short observation period.

V. Development of Real-Time Capability

Having demonstrated the capability of resolving the carrier phase ambiguity and obtaining 50- to 100-nrad angular accuracies, the subsequent goal is to demonstrate the capability to collect and process CEI data in real time. The two key components required to achieve this goal are a communications channel to bring the observed data to a common site and a real-time correlator to process the received signals. Over the past year, the authors have im-

plemented these components at Goldstone. Figure 4 shows a block diagram of the entire Goldstone real-time CEI system. The existing Mark III wide-channel-bandwidth VLBI data acquisition terminals (DATs) at each station are used to perform the downconversion, sampling, 1-bit quantization, time tagging, and formatting of the radio signal at each site. However, instead of recording the resulting bit stream on tape, the signals from DSS 15 are sent via a digital fiber-optic link to DSS 13. There, a real-time correlator, based on the architecture of the non-real-time JPL/Caltech Block II VLBI correlator, receives the signals from both stations and performs cross-correlation processing.

A. Fiber-Optic Data Link

The fiber-optic link, shown in Fig. 5, consists of two main units: a transmitter unit and a receiver unit. Commercially available equipment was used to the fullest extent possible to minimize development costs. The optical fiber itself exhibits very low dispersion and low losses. The measured end-to-end attenuation of the optical signal from DSS 15 to DSS 13 is −16 dB. Previous dispersion measurements of a 14-km length of this fiber placed an upper limit of 1 deg of phase nonlinearity over a 50-MHz bandwidth [8].

The transmitter unit is located at the remote site where it collects the Mark III data and transmits them through the fiber-optic cable to the site where the real-time correlator is located. The transmitter is composed of three main building blocks. The first of these, the interface circuitry, converts from the balanced emitter-coupled logic (ECL) voltage levels of the Mark III DAT to transistor–transistor logic (TTL) levels. The second stage of processing, based on the AMD TAXI AM7968 high-speed multiplexor chip, takes the parallel VLBI data (14 channels × 4.5 Mbit/sec) and encodes them by using a 4/5 encoding scheme, converting them to a serial data stream with synchronization words inserted. Finally, this serial bit stream is sent to a laser module where the signal is converted to light levels sent across the optical fiber to the receiver site. The optical transmitter (PCO DTX-13-565) modulates the data onto a 1300-nm optical carrier signal, with −3-dBm power. The aggregate bit rate on the fiber-optic link is 125 Mbit/sec.

The receiver is also composed of three main building blocks. The first of these is the pin diode receiver/comparator (PCO RTX-13-565) with −33-dBm sensitivity; here the signal is converted back to an ECL signal. This signal is then sent to a serial-to-parallel converter/decoder (AMD AM7968) where the bit stream is synchronized, decoded (5/4), and made available as a parallel word, along with strobe and status bits. The last stage converts the TTL signals back into the balanced ECL signals required by the correlator.

B. Real-Time Correlator

The real-time correlator, dubbed Real-Time Block 2 (RTB2) is a subset of the JPL/CIT Block II VLBI processor used for non-real-time processing of VLBI data. The RTB2 provides processing for 2 stations, 1 baseline, and 14 channels, while the full JPL/CIT Block II handles up to 4 stations, 6 baselines, and 28 channels. The large wirewrap boards comprising the system are identical to those in the Block II, and the VAX software is common to both processors. The output data files are identical to those of the Block II, and all the Block II postprocessing software can be used for RTB2. The Block II itself can be arranged to be the same as RTB2 with a quick cable change, facilitating the testing of new software on the Caltech campus, rather than in the operational machine. The system is built in a single rack and, of course, has no tape playback units. A brief description of the system follows.

An overview of the correlator is shown in Fig. 6. Standard Mark III formatted data enter RTB2 on two ribbon cables, which are the same as those that would normally go to a Honeywell 9600 tape recorder in a Mark III VLBI DAT. One of these will normally come from the local formatter and the other from a remote formatter via a fiber-optic link. Data from the two sets of 14 "tracks" first enter bit synchronizers that recover the data and clock signals and then pass to a 28-by-28 crossbar switch that can be set by the user to connect any track to any correlator channel. The 14 tracks from the local station are connected to channels 1–14 and those from the remote station to channels 15–28. The data are then passed through digital delay lines that are driven by 28 separate delay models sent from the VAX to the station processor. The output of the delay lines is fed to both the tone extractor board and the cross-correlator board. On the tone extractor board, there is one tone extractor for each channel, but it is time-multiplexed to allow four different tones to be extracted from each channel, and hence there are 112 different phase polynomial tone models sent by the VAX to the station processor. The connections from the delay lines to the cross-correlator board are arranged to correlate the first 14 channels with the second 14 channels. The user can choose to correlate 14 channels with 8 lags each, 7 channels with 16 lags each, or 1 channel of 112 lags. The last case would normally be used for searching clock delay with a delay range of 28 μsec. The cross-correlation board is driven by 14 phase models and 14 fractional delay mod-

els for each of the two antennas sent by the VAX to the correlator processor.

The RTB2 retains all the features of the Block II, including spectral domain fractional bit correction. Normal integration times are integral seconds. To the user, the system appears as a two-station 14-channel correlator. The correlator control file (or keyboard commands) are the same as would be used for configuring and controlling the Block II by using two tape transports. The output file also appears to be the result of a Block II correlation using two tape transports. The monitor/display system runs on a VAX workstation and uses a second copy of the output file sent over the EtherNet, just as in the Block II system. The display shows, in real time, the state and quality of the data being received from each station, plots of the correlation fringes for all channels versus time, plots of the phases of all tones for one channel versus time, and plots of the integrated delay and delay rate patterns for one channel. The information to be displayed is chosen by the user with a mouse-driven graphics interface. Additional real-time features, including spacecraft tone acquisition and tracking, could be added in the future.

VI. Results and Future Plans

On June 18, 1991, the first end-to-end test of the Goldstone CEI system was performed. Observations of the Magellan spacecraft were scheduled on the DSS-13–DSS-15 baseline, concurrent with a regularly scheduled Magellan telemetry pass at DSS 15. Fringes were successfully detected that corresponded to the cross-correlation of the Magellan carriers at 2.3 and 8.4 GHz. Figure 7 shows the first detected fringes.

This initial test served to verify the end-to-end processing of the Goldstone CEI system and demonstrated the digital fiber-optic link and the real-time correlation processing capabilities. To verify the angular accuracy of the observables, differential quasar pair observations were scheduled on October 3, 1991. From 03:29:00–04:17:00 GMT, the two quasars 3C 454.3 and CTA 102 were observed at S-band and X-band. These two sources are separated by 6.8 deg on the plane of the sky. Twelve 3-minute scans were scheduled, alternating between sources. Fringes were visible in real time at the RTB2 correlator during data acquisition. Postprocessing of the correlated phase data yielded the ambiguity-resolved S-/X-band calibrated phase delay residuals shown in Fig. 8. An uncertainty of 7 psec was assigned to each scan to reflect the expected level of troposphere fluctuations, based on the model of [5,6].

These residuals were then fit to estimate the relative angular position of 3C 454.3 relative to CTA 102. Given the limited duration of this data arc, the baseline projection on the plane of the sky did not rotate through a large angle, and as a result these data alone were not adequate to estimate both components of the angular separation of the sources. Instead, due to the predominantly north–south orientation of the baseline, just the declination of the source 3C 454.3 was estimated. The position of each source is known from regular VLBI observations to an accuracy of 5 nrad, providing a truth model against which the CEI determination can be compared. The twelve observations were grouped into four sets of three scans. For each A-B-A sequence, a clock epoch and rate were fit. This served to interpolate the A observations to the epoch of the B observation and removed any constant or linear error in the phase delay. For the entire set of observations, the declination of 3C 454.3 was fit, with no a priori constraint. In addition, the relative zenith troposphere and the baseline vector components were estimated, all with 1-cm a priori constraints. These parameters were included so that the final formal error in declination would reflect potential uncertainties in station-differenced troposphere and station location. The resulting adjustment to the a priori declination of 3C 454.3 was 90 ± 88 nrad. The adjustments to the troposphere and baseline vector were small, as compared with their a priori 1-cm constraints.

Further observations of close quasar pairs to demonstrate the astrometric accuracy of the CEI system will be conducted in the near future. Other potential demonstration opportunities include observing the Galileo, Magellan, or Ulysses spacecraft. In particular, accurate angular tracking of Ulysses during its Jupiter Gravity Assist, conducted in February 1992, would help to improve the Jupiter ephemeris in the radio reference frame. This, in turn, could benefit the approach navigation for Galileo, which arrives at Jupiter in 1995. To this end, CEI observations were collected at Goldstone during the Ulysses flyby of Jupiter. Analysis of these data is currently under way. Preliminary indications suggest that angular accuracies on the order of 50 nrad will be achieved.

VII. Conclusions

A real-time CEI capability has been developed and demonstrated at the Goldstone Deep Space Communications Complex on the 21-km baseline between DSS 13 and DSS 15. The key technology developments that enabled this demonstration are a high-rate digital fiber-optic link and a real-time correlation processor. The fiber-optic link

carries digitized, time-tagged data at an aggregate bit rate of 125 Mbit/sec from SPC 10 to DSS 13. The correlator, based on the JPL/Caltech Block II VLBI processor, supports cross-correlation of up to 14 2-MHz channels of Mark-III formatted VLBI data, and allows extraction of calibration and/or spacecraft tone signals. Real-time data have been successfully acquired for both spacecraft and quasar observations. The RTB2 system displays interferometric fringe data in real time, providing verification of successful data acquisition. Differential quasar pair observations have been performed, achieving angular accuracies of under 100 nrad for less than 1 hour of data.

Acknowledgments

The authors thank George Lutes for his assistance and expertise in the area of fiber optics; Lyle Skjerve, Ben Johnson, and the entire staff of DSS 13 for their efforts in installation and data acquisition at Goldstone; and George Resch for his early encouragement in pursuing this work.

References

[1] W. M. Baars, J. F. van der Brugge, J. L. Casse, J. P. Hamaker, L. H. Sondaar, J. J. Visser, and K. J. Wellington, "The Synthesis Radio Telescope at Westerbork," *Proc. IEEE*, vol. 61, pp. 1258–1266, 1973.

[2] G. Davies, B. Anderson, and I. Morison, "The Jodrell Bank Radio-Linked Interferometer Network," *Nature*, vol. 288, pp. 64–66, 1980.

[3] A. R. Thompson, B. G. Clark, C. M. Wade, and P. J. Napier, "The Very Large Array," *Astrophys. J. Suppl.*, vol. 44, pp. 151–167, 1980.

[4] M. J. Batty, D. L. Jauncey, P. T. Rayner, and S. Gulkis, "Tidbinbilla Two-Element Interferometer," *Astron. J.*, vol. 87, p. 938, 1982.

[5] C. D. Edwards, "Angular Navigation on Short Baselines Using Phase Delay Interferometry," *IEEE Transactions on Instrumentation and Measurement*, vol. 38, p. 665, 1989.

[6] R. N. Treuhaft and G. E. Lanyi, "The Effect of the Dynamic Wet Troposphere on Radio Interferometric Measurements," *Radio Science*, vol. 22, pp. 251–265, 1987.

[7] C. D. Edwards, "The Effect of Spatial and Temporal Wet-Troposphere Fluctuations on Connected Element Interferometry," *TDA Progress Report 42-97*, vol. January–March 1989, Jet Propulsion Laboratory, Pasadena, California, pp. 47–57, May 15, 1987.

[8] G. Lutes and A. Kirk, "Reference Frequency Transmission Over Optical Fibers," *TDA Progress Report 42-87*, vol. July–September 1986, Jet Propulsion Laboratory, Pasadena, California, pp. 1–9, September 15, 1987.

[9] C. D. Edwards, "Development of Real-Time Connected Element Interferometry at the Goldstone Deep Space Communications Complex," paper AIAA 90-2903 presented at the AIAA/AAS Astrodynamics Conference, Portland, Oregon, August 20–22, 1990.

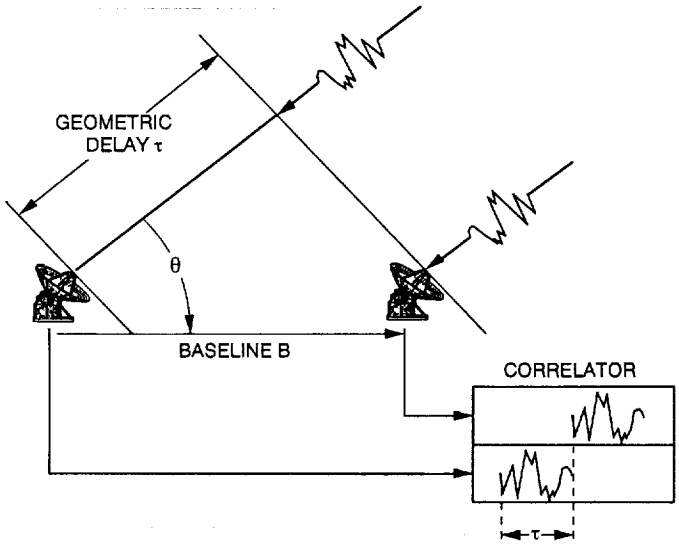

Fig. 1. Cross-correlation of signals received at two stations allows determination of the delay in arrival times of the signal wavefront at the two sites, which in turn determines the angle of the radio source relative to the baseline vector between antennas.

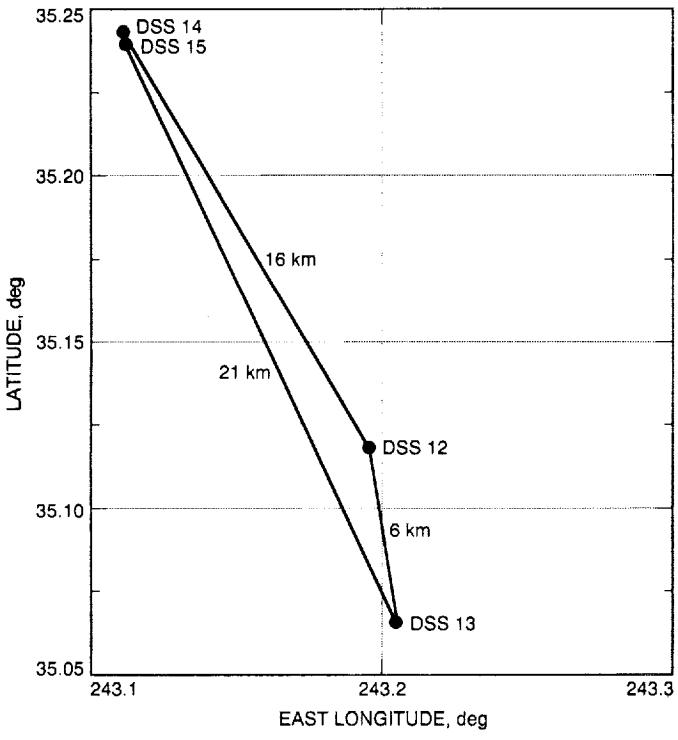

Fig. 2. Existing antennas and CEI baselines at the Goldstone DSCC.

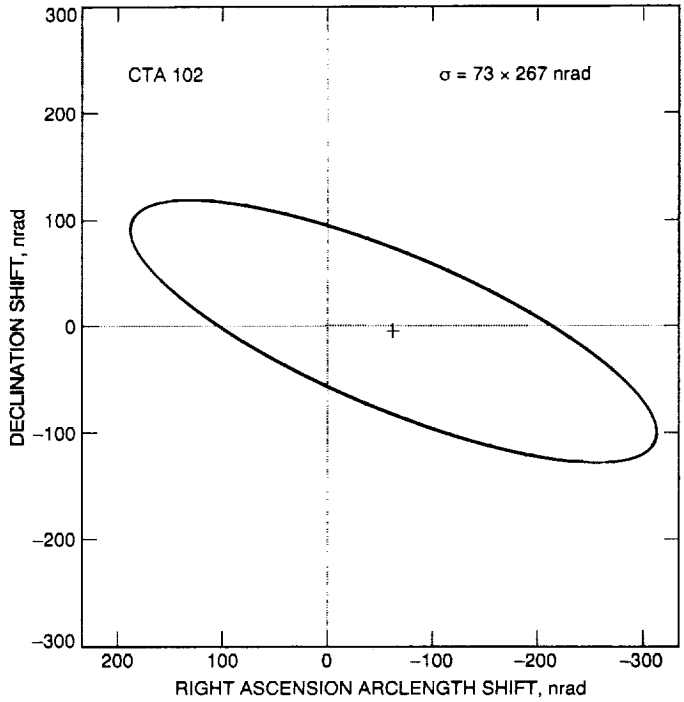

Fig. 3. Angular accuracy achieved for a non-real-time phase delay experiment on the 21-km DSS-13–DSS-15 baseline.

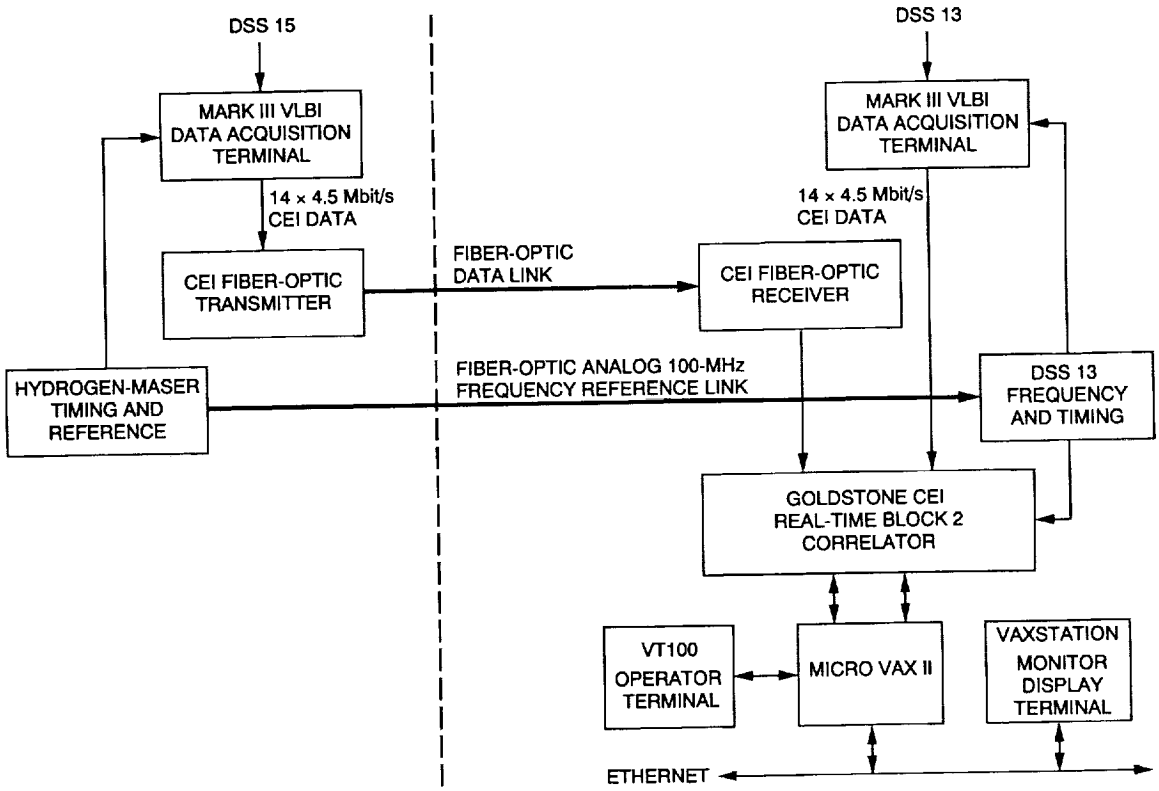

Fig. 4. Goldstone real-time CEI block diagram.

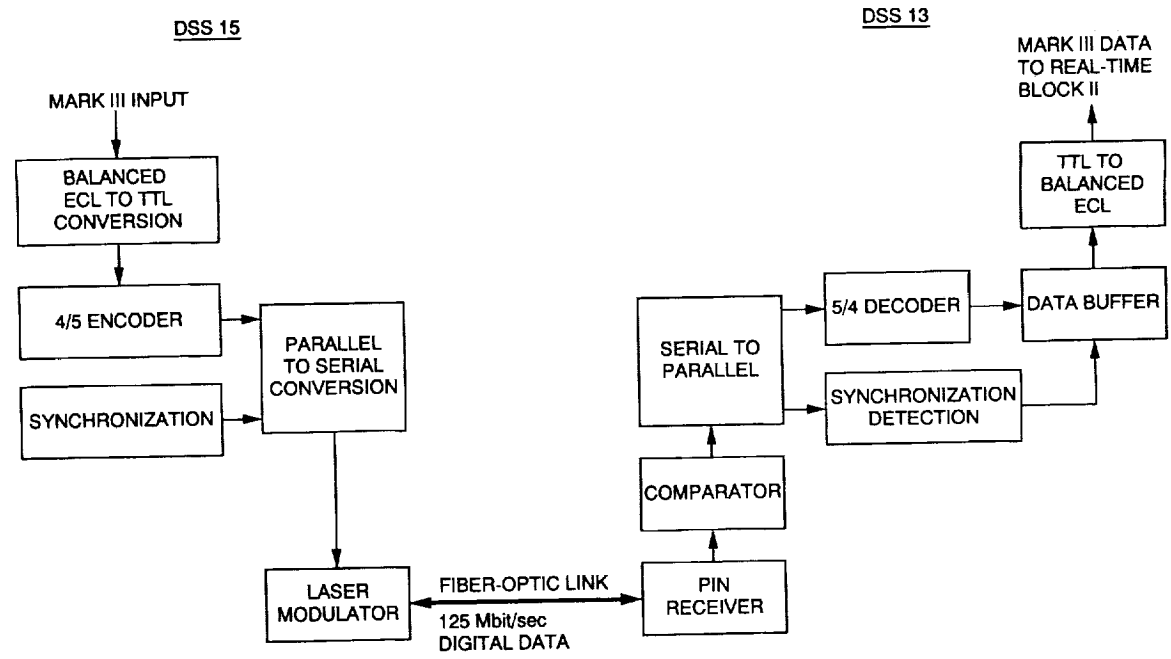

Fig. 5. Fiber-optic digital data link block diagram.

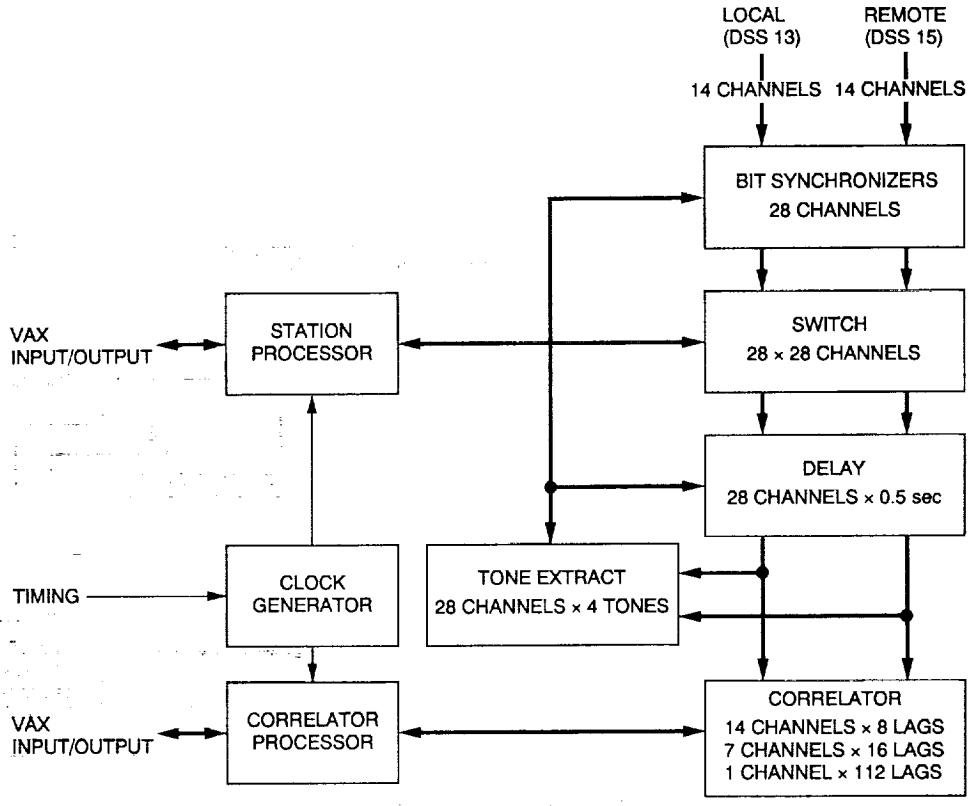

Fig. 6. Block diagram of the real-time Block II correlator.

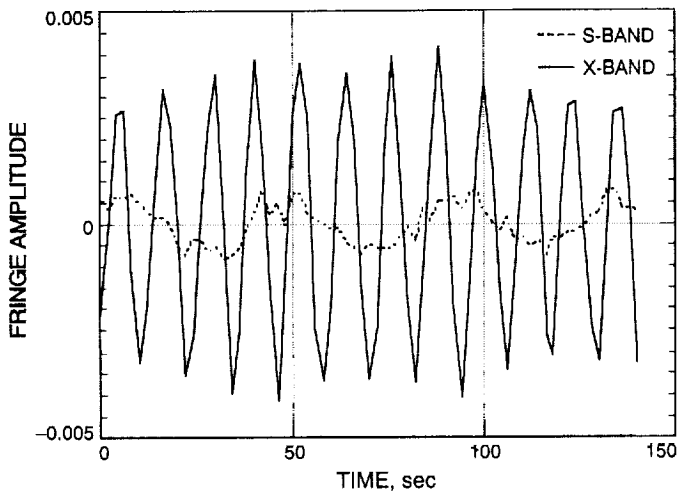

Fig. 7. First real-time fringes obtained on the Goldstone real-time CEI.

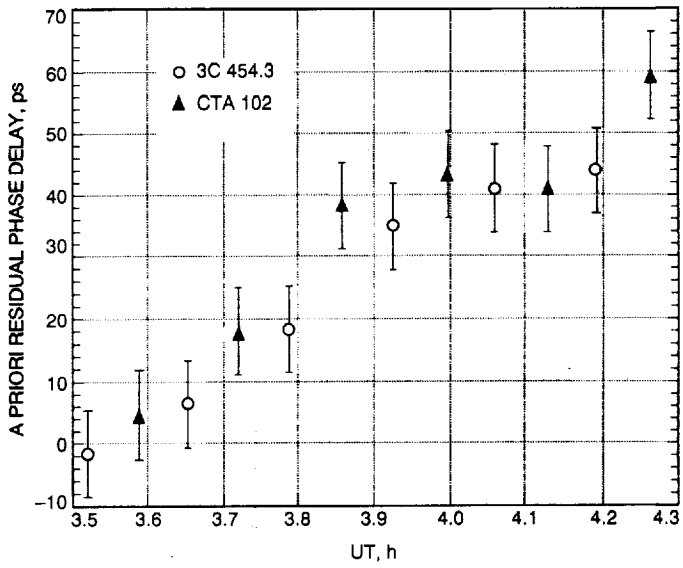

Fig. 8. Phase delay residuals for October 3, 1991, CEI observations of the radio source pair 3C 454.3–CTA 102 between DSS 13 and DSS 15.

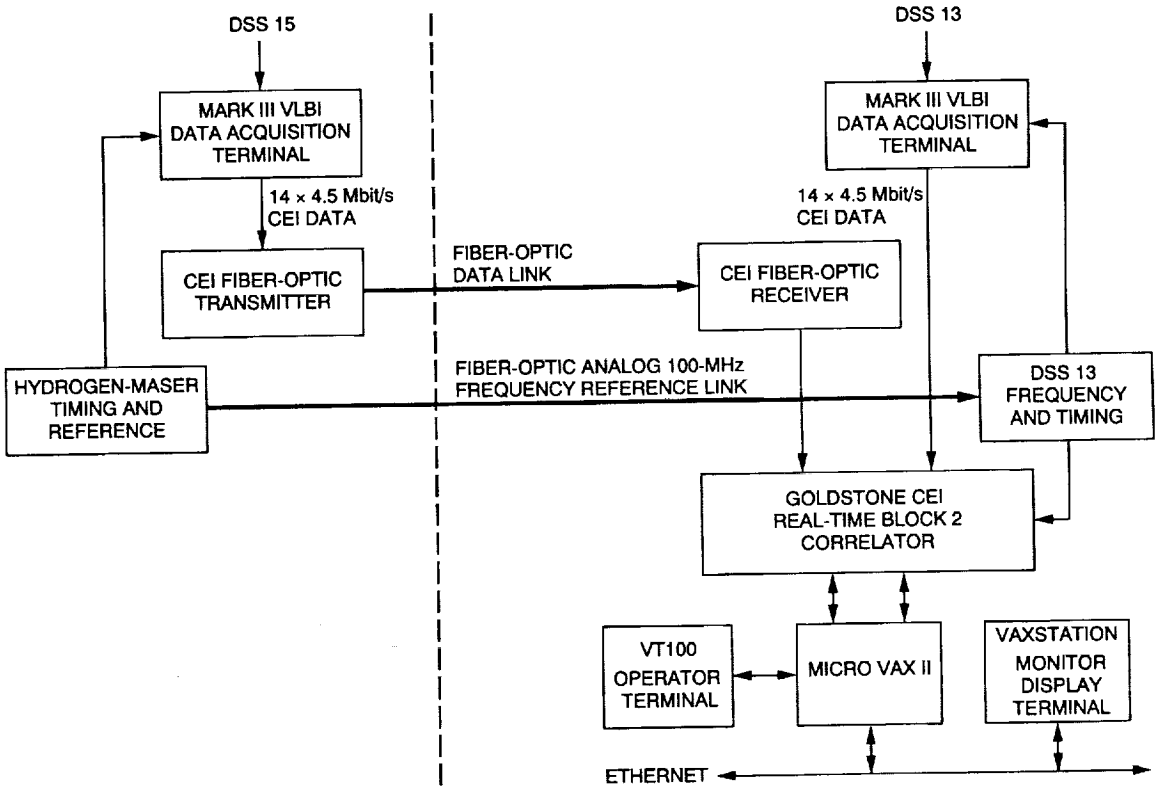

Fig. 4. Goldstone real-time CEI block diagram.

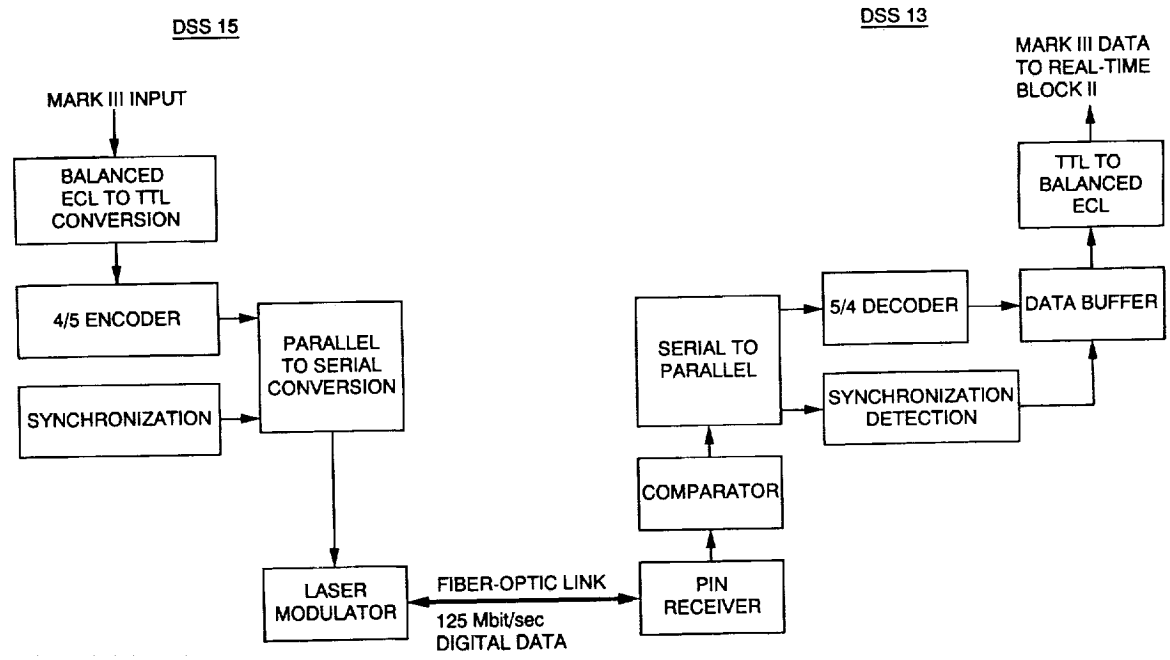

Fig. 5. Fiber-optic digital data link block diagram.